![University of Leeds]

UNIVERSITY OF LEEDS

This is a repository copy of *Revealing the superior corrosion protection of the passive film on selective laser melted 316L SS in a phosphate-buffered saline solution*.

White Rose Research Online URL for this paper:
https://eprints.whiterose.ac.uk/162886/

Version: Accepted Version

![White Rose university consortium — Universities of Leeds, Sheffield & York]

eprints@whiterose.ac.uk
https://eprints.whiterose.ac.uk/

Revealing the superior corrosion protection of the passive film on selective laser melted 316L SS in a phosphate-buffered saline solution

Xiaoqi Yue[a, b, e], Lei Zhang[a], Yong Hua[b]*, Jian Wang[c], Nan Dong[c], Xueda Li[d], Shusheng Xu[b] and Anne Neville[b]

a: Institute for Advance material and Technology, University of Science and Technology Beijing, 30 Xueyuan Road, Beijing, China.
b: Institute of Functional Surfaces, School of Mechanical Engineering, University of Leeds, Leeds, LS2 9JT, United Kingdom.
c: School of Material Science and Engineering, Taiyuan University of Technology, Taiyu an, Shanxi, China.
d: School of Mechanical and Electronic Engineering, China University of Petroleum, Qingdao, Shandong, China.
e: Shunde Graduate School, University of Science and Technology Beijing, Shunde, China.

*Corresponding author: Yong Hua, Email: Y.Hua@leeds.ac.uk;

Abstract

This study investigated the passivation behaviour of wrought 316L stainless steel (SS) and 316L manufactured by the Selective Laser Melting (SLM) process in phosphate-buffered saline (PBS). The 3D printing laser power influenced microstructure, passive film and corrosion resistance of SLM 316L SS were studied, and compared with the results of wrought 316L SS. The results indicated that a smaller corrosion current density and improved breakdown potential (E_b) of SLM 316L SS was associated with a higher proportion of Cr_2O_3 in the passive film at OCP conditions. The Transmission Electron Microscopy (TEM) proved that the passive film on SLM 316L SS was continuous and compact at 600 mV vs. Ag/AgCl applied potential. The increase in the applied potential resulted in a high content of hydroxide being recorded in the passive film. The results also suggest preferential facets of (110) and abundant grain/sub-grain boundaries for SLM 316L SS, as well as the increased work of separation and growth rate of the passive film from the substrate. Wrought 316L SS demonstrated preferred facets of (111)-γ and larger grains. There are confirmed via X-Ray Diffraction (XRD), Electron Backscatter Diffraction (EBSD) and the first-principle calculation.

1. Introduction

Recently 316L austenitic SS was considered as a biological substitute material in orthodontics, orthopedics and dentistry based on its excellent corrosion resistance, good mechanical properties, as well as low cost [1–4]. However, the toxic effects of chromium and its compounds are important limitations if a particularly long design life is required for the application. The passivation stability under the environment in the presence of chloride ions [5] or fluoride ions [6], as well as the release of harmful ions such as Cr^{3+} and Ni^{2+}, are the two main focus topics for the material suitability. The European standard for the release rate of Ni for piercing post assemblies was limited within 0.2 $\mu g/(cm^2$ week) [7]. Nie et al. [8] indicated fine grain size with a nano-crystalline structure tended to have better corrosion resistance than large grain (micro-crystalline) structures in an artificial saliva solution. Similarly, Lv et al. [9] investigated the extra processing to improve the corrosion resistance of 316L SS in artificial saliva solution, finding both cryogenic cold rolling (to obtain a nano-crystalline structure) and electrochemical nitridation are effective ways. For the consideration of passive film recovery, Zhang et al. [10] investigated the passive film growth of 316L SS after a friction test and obtained a thickness of 2.33 nm after 15 minutes of potentiostatic polarization in the passive region. At free corrosion potential, Zijlstra et al. [11] indicated that the passive film recovery needs at least 2 hours using the in-situ AFM method. Similar results were observed by Kok et al. [12] who reported that the E_{corr} does not approach the initial E_{corr} value within 100 minutes, indicating that full recovery had not been reached. Considering the inevitable passive film damage on the substituted biological materials such as 316L SS caused by wear and tear, the required repassivation period will release harmful ions such as Cr^{3+} and restrict the application of 316L SS in biological field.

SLM technology has received considerable attention [13,14] because of the fast fabrication of individual parts and the ability to produce more complex components without expensive tooling and machining [15]. SLM now is expected to become one of the most popular manufacturing processes in the fabrication of biological components. SLM 316L SS made by using the powder bed fusion manufacturing process has its unique microstructure characterised by smaller grain sizes. This process allows it to have refined grains directly without further surface treatment [16]. Nevertheless, the rapid solidification during this manufacturing process for SLM 316 SS can cause the material to become porous [17], which promoted the initiation of pitting corrosion [18]. Moreover, Man et al.

64 [19,20] indicated that the increased sub-grain boundaries accompany higher dislocation density,

65 which would weaken the bonding of the interfaces between the passive film and the steel substrate

66 [21]. Secondly, the inclusions in the SLM 316L SS present different characteristics compared to those

67 in the wrought melted, not only in size but also in species [19]. Chao et al. [22] suggested that the

68 inclusion sizes observed from SLM 316L SS were over an order of magnitude smaller than those from

69 the wrought melted, and the composition was mainly Mn, Si, O, Al, and N, rather than sulfide-oxide

70 duplex inclusions, which are considered as the pitting initiation sites in the wrought 316L SS [23].

71 Researchers also studied the effects of solution segregation [24], residual stress [25,26], and special

72 grain directionality [27] on SLM 316L SS. The macrostructure characteristics and manufacturing

73 process of SLM 316L have recently been studied and reported significantly, but little is known about

74 the passivation properties of SLM 316L. Man et al. [19] and Kong et al. [28] reported the thickness

75 differences of the passive film between SLM 316L SS and wrought 316L SS using XPS. Their results

76 indicated the variation of hydroxide/oxide ratio in the passive film. However, the chemical

77 composition of the passive film reported no essential difference between wrought 316L SS and SLM

78 316L SS. Other electrochemical measurements indicated the different passivation and re-passivation

79 behaviour for SLM 316L SS and wrought 316L SS, but without further elaborating in detail [29,25].

80 Unfortunately, the relationship between passivation/re-passivation properties and passive film

81 characteristics is not clear for SLM 316L SS; there is still some uncertainty around the passive film

82 structure and the re-passivation ability.

83 In this study, the knowledge gap relating to the passivation behaviour of SLM 316L SS and wrought

84 316L SS is addressed through a study in a PBS solution at 37°C. The ion concentrations (NaCl, KCl and

85 KH_2PO_4) and the osmolarity within the PBS solution are close to what is seem in the human body

86 [17]. The role of the passive films on influencing the corrosion resistance of wrought and 3D printed

87 316L SS was investigated via both experiments and first-principle calculations. The characteristics of

88 the material microstructure, passivation stability, and the passive film compositions were analysed

89 by a combination of EBSD, Scanning Electron Microscopy (SEM), X-Ray Diffraction (XRD), X-ray

90 Photoelectron Spectroscopy (XPS), Focused Ion Beam (FIB), and Transmission Electron Microscopy

91 (TEM). The first-principle calculations were used to reveal the fundamental mechanisms in terms of

92 the passive film structure, binding energy and the work of separation between the passive film and

93 substrate, which aid to the understanding of the interface properties of wrought and 3D printed

94 316L SS.

95

2. Experimental Section

2.1 Material and methods

The 316L SS samples were manufactured using a traditional wrought process and SLM EOS M290 system, respectively. The 316 SS powders (15-45 μm in diameter) were selected for SLM manufacturing. The chemical compositions of materials are listed in Table 1. The SLM manufacturing was operated at a spot size of 0.08 mm and with a 1070 nm wavelength laser using a scan speed of 715 nm/s. SLM samples were scanned in a zigzag pattern with different powers (80 W and 200 W) to a thickness of 25 μm per layer. After each layer is produced done, the laser is rotated by 67° to reduce the stress concentration during manufacturing. All the samples were manufactured to a cylinder (15 mm of diameter) and then cut uniformly to the thickness of 5 mm. The grain size, grain boundaries, and grain orientation were observed using EBSD. The EBSD was carried out by OXFORD Nordlys MAX3 with a High-resolution CCD of 640 x 480. The grain structure and preferred grain orientation were analysed using an XRD system (Bruker D8) from 30° to 100°.

Table 1. Chemical composition of for wrought and powder 316L SS

Elements (wt%)	C	Cr	Mn	Si	P	S	Mo	Ni	N	Fe
Wrought 316L	0.03	17.5	2	1	0.045	0.03	2.5	13	0.11	Bal.
Powder 316L	0.02	16.8	1.9	0.1	0.032	0.02	2.25	12.1	0.15	Bal.

A PBS solution (pH = 7.4) was used and conveniently packaged pre-made Sigma-Aldrich buffer solutions with high quality. The chemical composition is provided in Table 2, all electrochemical studies were performed in PBS solution at 37 ± 0.2°C.

Table 2. Chemical composition of PBS solution

Salt	NaCl	KCl	Na_2HPO_4	KH_2PO_4
Concentration (mmol/L)	137	2.7	10	1.8

2.2 Electrochemical measurements

Potentiodynamic polarisation tests were measured to clarify the passivation behaviour. An ACM Gill workstation was used for all the electrochemical measurements. In a typical three-electrode system,

the working electrodes are the prepared wrought or SLM 316L SS samples; the counter electrode and reference electrode are a platinum foil and an Ag/AgCl electrode (3 mol/L KCl solution). All the working electrodes were sealed within a resin to leave one surface for exposure and polished with SiC paper down to 800# grit, followed by cleaning and drying. Before each test, samples were checked using a optical microscope to ensure there is no porosity or inclusions exposed on the surface to avoid the effect of porosity and inclusions on the passivation behaviour. The 316L SS samples was reached a steady-state after 3600 s. Subsequently, potentiodynamic polarisation sweeps were conducted over the potential range of -0.2 V and 1.4 V vs. OCP using a scan rate of 0.5 mV/s. For the potentiostatic polarisation tests, the air-formed film was removed by cathodic polarisation at -1.0 V vs. Ag/AgCl for 300 s, followed by applying the potential of 200 mV, 400 mV, and 600 mV vs. Ag/AgCl potentiostatic for 1000 s, respectively. Electrochemical Impedance Spectroscopy (EIS) tests were performed over a frequency range of 100 kHz~10 mHz using an amplitude sinusoidal voltage of 10 mV at OCP, 200 mV, 400 mV, and 600 mV vs. Ag/AgCl respectively.

2.3 Surface analysis

Before surface analysis, the samples were removed from the three-electrode system after the potentiostatic polarisation tests, dried and stored in a vacuum desiccator. XPS with a monochromatic X-ray source (Al kα radiation source, hv = 1486.6 eV and operated at 150 W) was used to identify the high resolution of O, Ni, Cr, Fe and Mo products within the passive film. The cross-sectional TEM images of the passive film were prepared using FIB (NOVA200) at accelerating voltages between 30 and 5 kV using beam currents between 5 and 0,1 nA. The image of the passive film was characterized using TEM (Technai F20 FEGTEM by FEI operated at 200 kV), and the chemical composition of the passive film was investigated by EDX (Gatan Orius SC600 CCD camera) with Cs-corrected STEM.

2.4 First-principle calculations

Based on the density functional theory (DFT), first-principle calculations were used to calculate the work of separation (W_{sep}) between the passive film and steel substrate. To simplify the model of 316L SS and the passive film, Fe and Cr_2O_3 were used, respectively. Accordingly, a 1 x 1 x 3 supercell was constructed for the interface between the Fe (Cambridge crystallographic data centre, CCDC) and Cr_2O_3 (inorganic crystal structure database, ICSD). Based on the interface model proposed by CASTEP (Ambridge Sequential Total Energy Package), the pure Fe in (110) and (111) cleave surfaces and the oxide Cr_2O_3 in (0001) cleave surface were chosen.

The generalized gradient approximation (GGA) exchange-correlation energy functional was used

151 with the Perdew-Burke-Ernzerhof (PBE) method and the Kurdjumov-Sachs (KS) relationship. The

152 ultrasoft pseudopotential (USPP) was performed to describe the effective parameter of interaction

153 between electrons and ion core, and the cutoff energy is 340 eV for a plane-wave basis. The ionic

154 relaxation was considered as convergence when the total energies below 10^{-5} eV, the force on every

155 atom is less than 0.03 eV/Å, and the displacements are lower than 10^{-4} nm.

156

3   Results

3.1 Characteristics of the material microstructure

159 EBSD was used to determine the microstructure of the steels; the results as shown in Figure 1

160 confirm that the wrought 316L SS has large and regular grains, whereas the SLM 316L SS has

161 relatively smaller and dissimilar grain sizes. The average grain size for wrought 316L SS was around

162 50 μm as shown in Figure 1b. Figure 1c and d show that the grain sizes of SLM 316L SS at 80 W laser

163 power have a wider range of 5-51 μm. For SLM 316L SS at 200 W laser power, the grain size turns to

164 increase and elongate along the construction direction. The results suggest that the formation of

165 large grains was attributed to the decreasing cooling temperature gradient with increasing laser

166 power.

167 The sub-grain boundaries that exist within SLM 316L SS were observed as light grey lines as shown

168 in Figure 1c and e. The colour changes within grains for SLM 316L as shown in Figures 1d and 1f

169 according to the changing in the crystal phase. The EBSD results indicate that the proportion of

170 crystal facets were mainly (110) by increasing the laser power to 200 W. Krishnan et al. [30] indicated

171 that the grains preferred to orient in a single direction at high laser beam power. From the colour

172 distribution shown in Figure 1f, the difference of grain orientation at 200 W was inconspicuous

173 compared with that at 80 W, which was consistent with previous research [28].


(a)   (b)
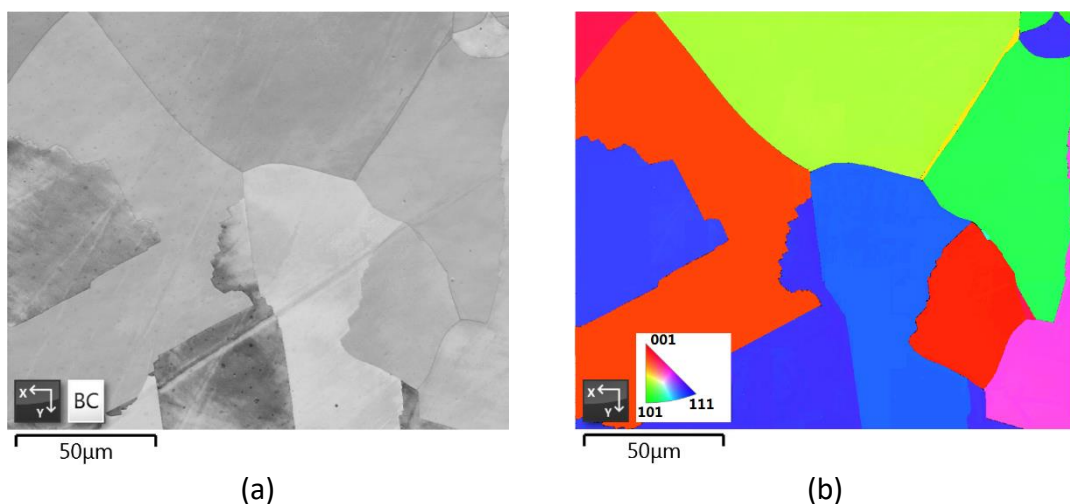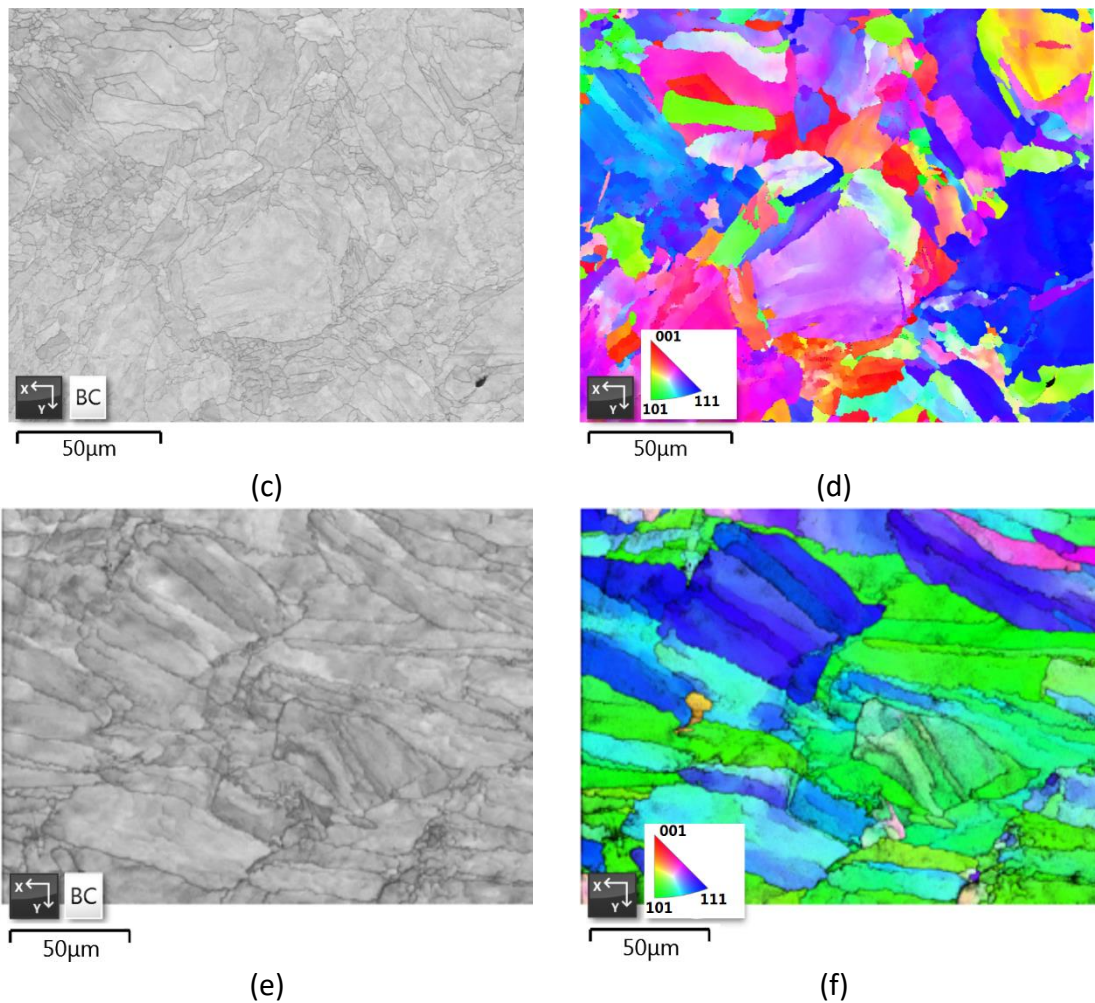
Figure 1. The EBSD results of the wrought and SLM 316L SS: (a) diffraction band contrast map and (b) IPF X map of wrought 316L SS, (c) diffraction band contrast map and (d) IPF X map of SLM 80 W 316L SS, (e) diffraction band contrast map and (f) IPF X map of SLM 200 W 316L SS.

The XRD patterns as shown in Figure 2 represent the γ austenite phase of (111), (200), (220), (311), and (222). The XRD patterns of the traditional wrought 316L SS and un-melted 316L SS powders indicate the most intense Bragg reflection for Fe relates to the (111) Miller plane, which is located at 2θ values of 44° and fixed-slit 100% from PDF database. Although for SLM 316L SS, the proportion of the peaks ((111) and (220)) varied, there were more γ-(220) grains in SLM 316L SS, especially with high laser power manufacturing at 200 W. These observations can be attributed to increased laser power which promotes a change in crystal phase from (111) (80 W) to (220) Miller plane (200 W). Besides, the EBSD results as shown in Figure 1 indicate that the 200 W sample contains a high fraction of (110) crystal facets. According to the research of Krishnan et al. [23], high laser power makes the austenite grains more inclined to orient in (110) facets, which was consistent with our results.
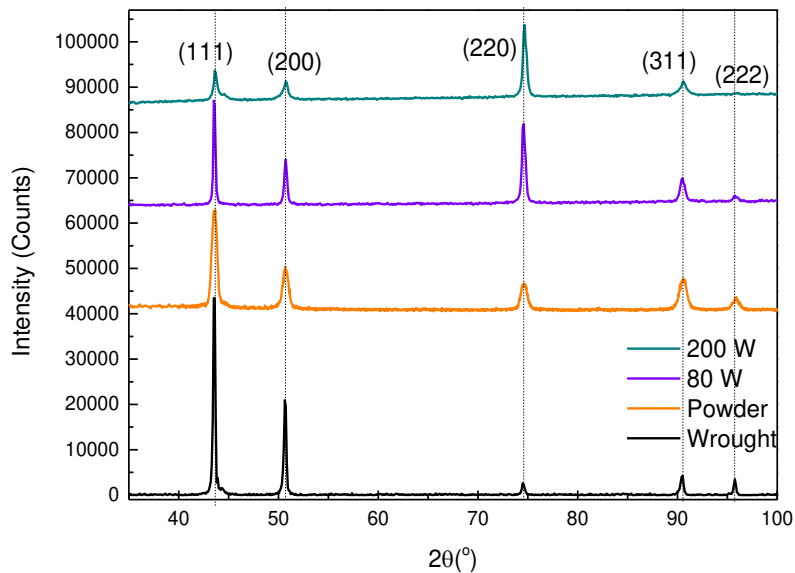
Figure 2. XRD patterns of the wrought, un-melted powder, SLM 316L SS at 80 W and 200 W.

3.2 Potentiodynamic analysis to characterise the passivation stability

Figure 3 shows the passivation behaviour of samples exposed to the PBS solution at 37°C. The open circuit potentials for all three materials were similar, around -110 mV. The E_b for both SLM materials was considerably higher (around 1100 mV vs. Ag/AgCl) compared to that of wrought 316L SS (around 430 mV vs. Ag/AgCl). A stable passive state with the passivation current density of 2 µA/cm² was recorded as increasing the laser power to 200 W. The results suggest that the SLM manufacturing affects passivation behaviour, especially in the high potential regions. The difference of passivation behaviour between SLM and wrought 316L SS no matter at OCP or high potential is closely associated with the structure or the chemical composition of the passive film formed on the surface.
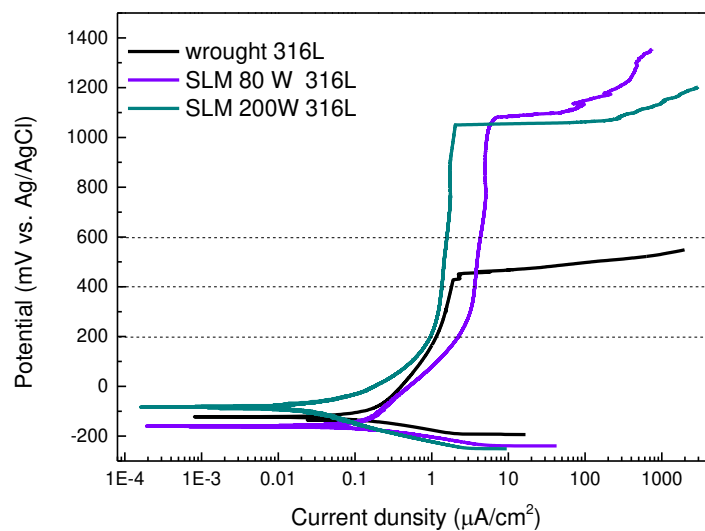
Figure 3. Potentiodynamic polarisation of wrought 316L SS and SLM 316L SS immersed in PBS solution.

To evaluate the passive film resistance at OCP, EIS experiments were recorded for the wrought and

205   SLM 316L SS samples exposed to the PBS solution as shown in Figure 4. The results of impedance

206   measurements show that SLM 316L SS at 200 W has the largest semi-circle which indicates the best

207   corrosion resistance. While the semi-circle of the wrought 316L SS sample was the smallest and

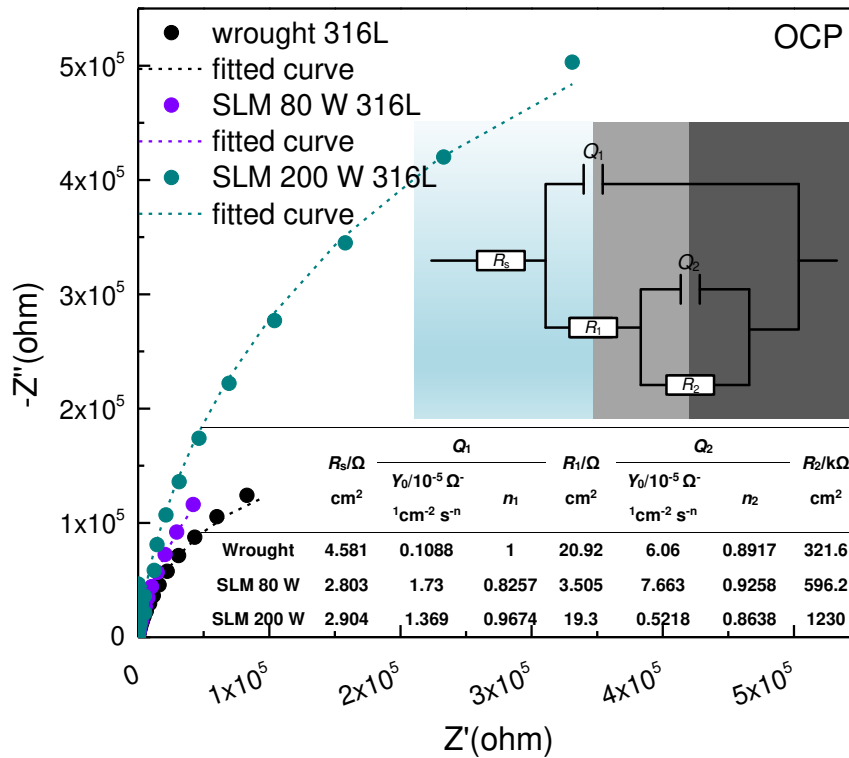208   indicates that the corrosion resistance of wrought 316L SS was inferior to that of SLM 316L SS.

209   The electrode-equivalent circuit was used to clarify the interpretation of electrochemical impedance

210   measurements such as interfacial phenomena or charge transfer impedance for wrought and SLM

211   316L SS. The results are provided in Figure 4, R_s is the solution resistance, R_1 and R_2 represent the

212   diffusion resistance and the charge transfer resistance, respectively. CPE1 (Q_1) is the capacitive

213   behaviour of the passive film at the outer interface between the solution and the passive film, and

214   CPE2 (Q_2) represents the inner interfaces. The impedance is defined via the following:

$$Z_Q = \frac{1}{(j\omega)^n Y_0} \tag{1}$$

216   where j is an imaginary number (j^2=1), ω is the angular frequency, n is the exponent which lies in the

217   region between 0 and 1, and Y_0 is the modulus. The CPE describes a Warburg impedance at $n = 0.5$

218   and an ideal capacitor at $n = 1$. In other cases, where $0.5 < n < 1$, the CPE represents a distribution

219   of dielectric relaxation times in frequency space.

220   The acquired modeling results are shown as dashed lines in Figure 4 and indicate good accordance

221   with the measured data. As listed in Figure 4, the diffusion resistance R_1 of the passive film for SLM

222   316L SS and wrought 316L SS was affected by the ion dissolution associated with the substantially

223   increased sub-grain boundaries [31,32]. The R_1 values for SLM 316L SS are not significantly different

224   compared to the wrought 316L SS in the PBS solution. However, the increase in R_2 values determines

225   the improved corrosion resistance for SLM 316L SS. It suggests the low-frequency time constant is

226   composed of Q_2 and R_2 mainly determines the better passive film behaviour [19,28]. The values of

227   Q_2 and R_2 indicate the corrosion processes at the inner interfaces, the smaller R_2 and bigger Q_2 values

228   suggest the corrosion processes at the inner interfaces were more heterogeneous. It is interesting

229   to note that R_{tot} values (Equation 2) for SLM 80 W and 200 W 316L were 596 kΩ and 1230 kΩ

230   respectively, which were substantially larger compared to 322 kΩ for wrought material, suggesting

231   that the SLM 316 SS given better corrosion resistance compared to that of the wrought 316L SS at

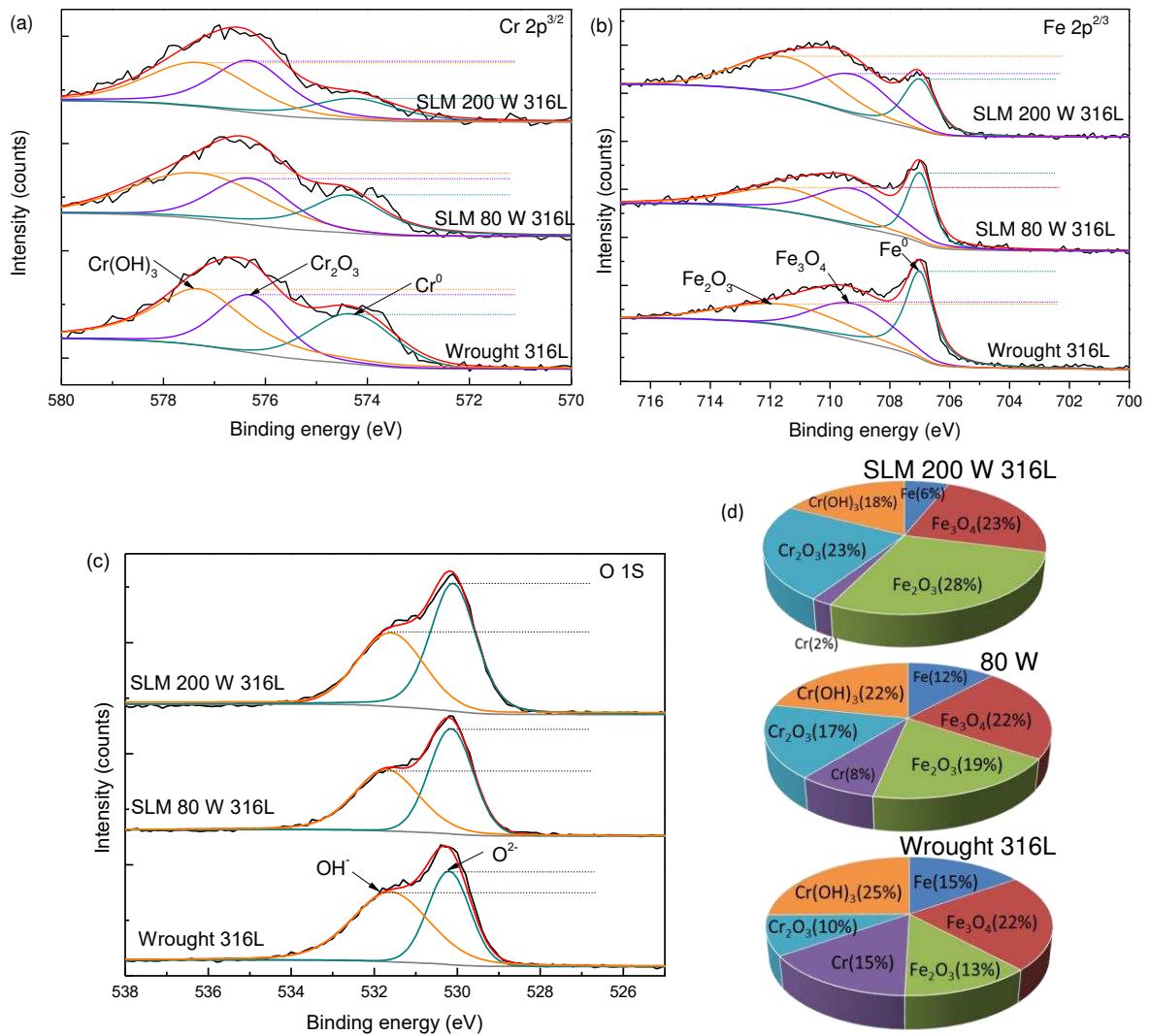232   OCP conditions in the PBS solution.

$$R_{tot} = R_1 + R_2 \tag{2}$$

Figure legend (in plot):
- wrought 316L — fitted curve
- SLM 80 W 316L — fitted curve
- SLM 200 W 316L — fitted curve

OCP

Embedded table in figure:

	$R_s/\Omega\ cm^2$	Q_1		$R_1/\Omega\ cm^2$	Q_2		$R_2/k\Omega\ cm^2$
		$Y_0/10^{-5}\ \Omega^{-1}cm^{-2}\ s^{-n}$	n_1		$Y_0/10^{-5}\ \Omega^{-1}cm^{-2}\ s^{-n}$	n_2	
Wrought	4.581	0.1088	1	20.92	6.06	0.8917	321.6
SLM 80 W	2.803	1.73	0.8257	3.505	7.663	0.9258	596.2
SLM 200 W	2.904	1.369	0.9674	19.3	0.5218	0.8638	1230

Figure 4. The EIS spectra of wrought 316L SS and SLM 316L SS immersed in PBS solution at OCP.

3.3 Characterisation of the passive films

The passive film composition on the surface was identified using XPS after immersion in PBS solution for 48 hours. Figure 5 represents the peaks of Cr-2p 2/3, Fe-2p 2/3, and O-1s. The Cr peaks were mainly located at 574.4, 576.3, and 577.3 eV, assigned to the Cr metallic state, Cr_2O_3, and $Cr(OH)_3$, respectively [19,28,33]. There were three peaks at around 711.4 eV, 709.2 eV, and 707 eV, suggesting the presence of Fe_2O_3, Fe_3O_4, and Fe [34–36]. The peaks of O 1s indicate the passive film formed on SLM materials contain higher oxide contents compared to that of wrought material. Figure 5c confirmed the lower proportion of Cr compounds within the passive film formed on the wrought 316L SS, the higher hydroxide and lower Cr_2O_3 contents compared to that of SLM 316L SS at 200 W. The work done by Maurice et al. [37], who used scanning tunnelling microscopy to study the passive film properties, indicated that the Cr atoms formed a film along the original grain orientation, where requires OH groups or combination of iron oxide into the network for structural relaxation. Their results pointed out that few OH groups and little opportunity for structural relaxation cause a denser ring network of Cr_2O_3.

Figure 5. XPS results of the passive film formed on the wrought and SLM produced 316L SS in PBS solution: (a) Cr-2p 3/2, (b) Fe-2p 3/2, and (c) O-1s and (d) quantitative analysis.

3.4 TEM observations of the passive films at OCP condition.

3.4.1 Wrought 316L SS

Figure 6 indicates the elemental compositions of the passive film formed on the wrought 316L SS, the thickness at the OCP condition was about 6.25 nm. Region A, B, and C represent the sputtered-coated Pt layer, passive film, and the metal substrate, respectively. The Fast Fourier Transform (FFT) pattern from region C indicated the Face-Centered Cubic (FCC) SS matrix at a plane of (111), which was consistent with EBSD and XRD results. The selected region B showed the passive film has no lattice phase contrast and suggests it has an amorphous-like structure.

Figure 6b shows the corresponding STEM and EDS mapping profiles of the passive film. Within the amorphous passive film, there is a high concentration of iron, oxygen, chromium and nickel. To further analyse the elemental composition within the amorphous passive film, an EDS line scan

across the entire passive film (the red arrow in Figure 7) was performed. The inner passive film was enriched in oxygen. The XPS results and the EDS line-scan throughout the passive film suggest that the metallic phase mainly consists of Fe and Cr with a small amount of Ni for wrought 316L SS.
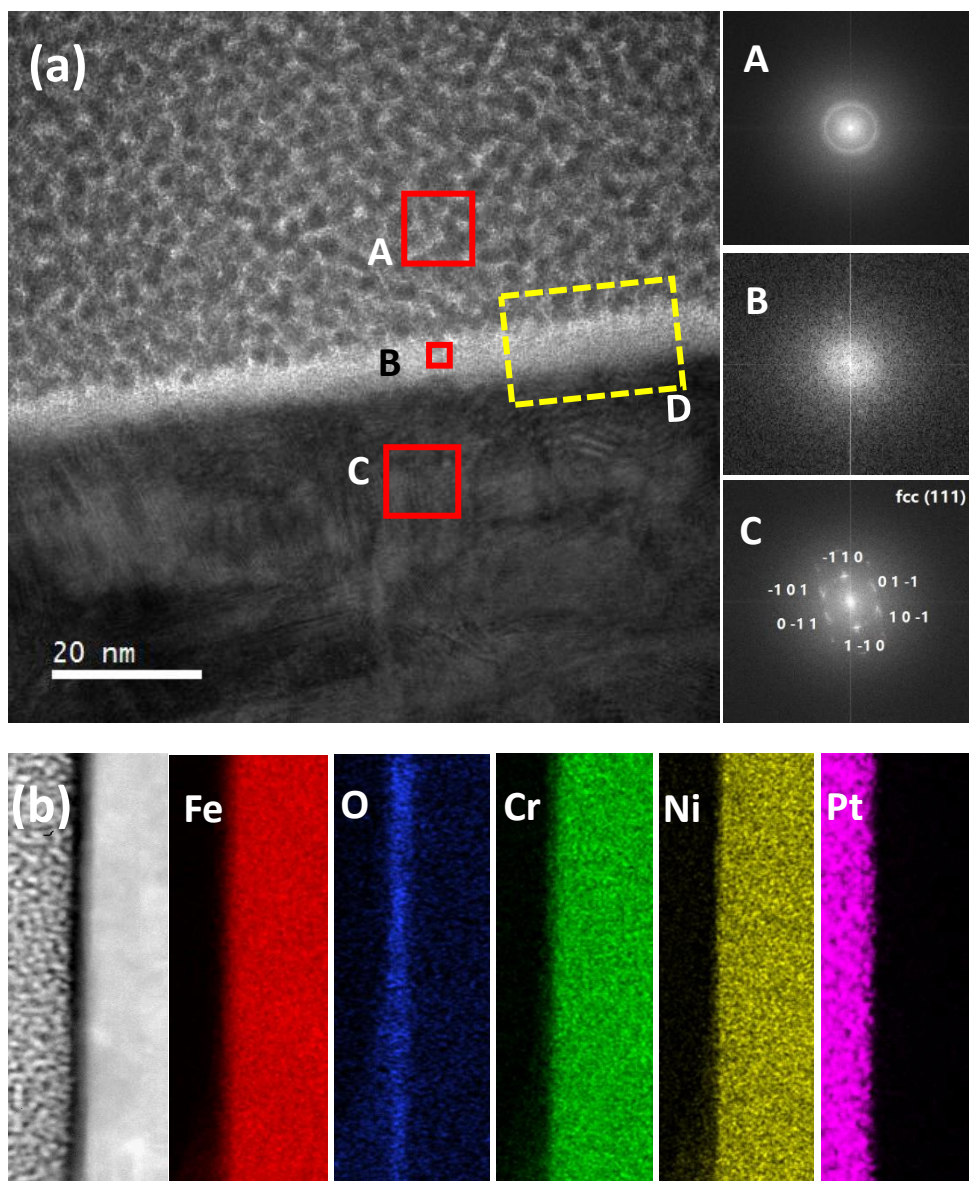
Figure 6. (a) An HR-TEM image of wrought 316L SS specimen in PBS solution at OCP, (b) a bright-field TEM image of the yellow square D in panel a and a STEM-EDX mapping profile of main matrix elements (Fe, O, Cr, Ni, Pt).
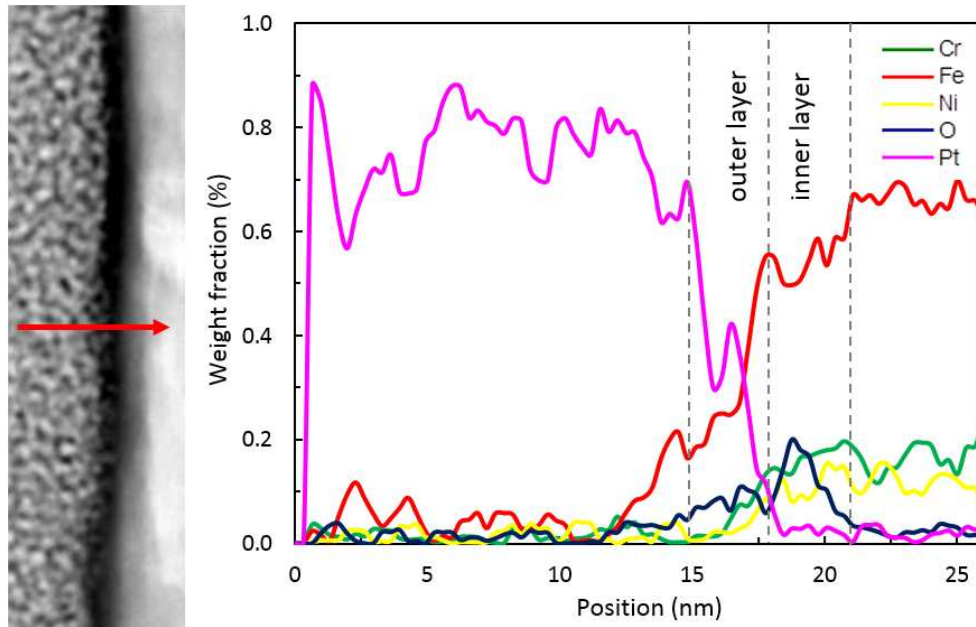
Figure 7. STEM image and EDS line profiles along the red arrow in the STEM image of the cross-sectional TEM sample of the wrought 316L at OCP in PBS solution.
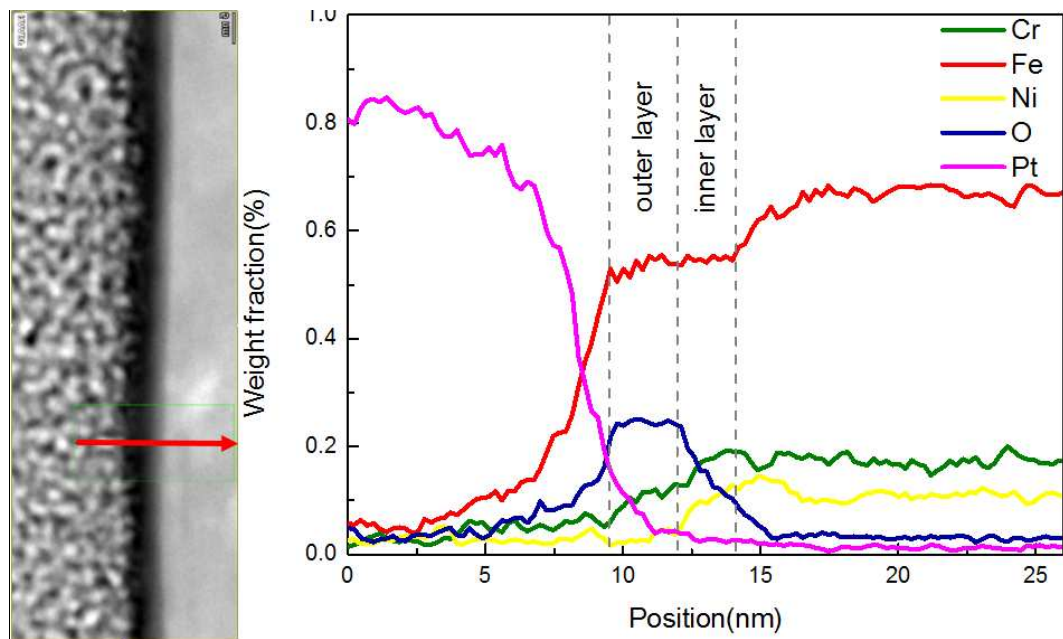
3.4.2 SLM 200 W 316L SS

The passive film structure and the elemental compositions on the SLM 316L SS at 200 W laser power surface were analysed by TEM as shown in Figure 8. The passive film at OCP conditions was slightly thinner, around 4.6 nm in thickness. The FFT pattern within region C (metal substrate) indicated the FCC stainless steel matrix at a plane of (110), which was consistent with EBSD and XRD results. The selected region B showed the passive film has no lattice phase contrast and suggests it is also amorphous-like in a compactable way to the wrought material.

Figure 8b shows the corresponding STEM and EDS mapping profiles of the cross-sectional TEM sample. High oxygen concentration was detected within the passive layer. It is noteworthy that a lack of iron was detected in the inner passive layer, while it contains high nickel and chromium, which is in agreement with the observations by Olefjord et al. [38].
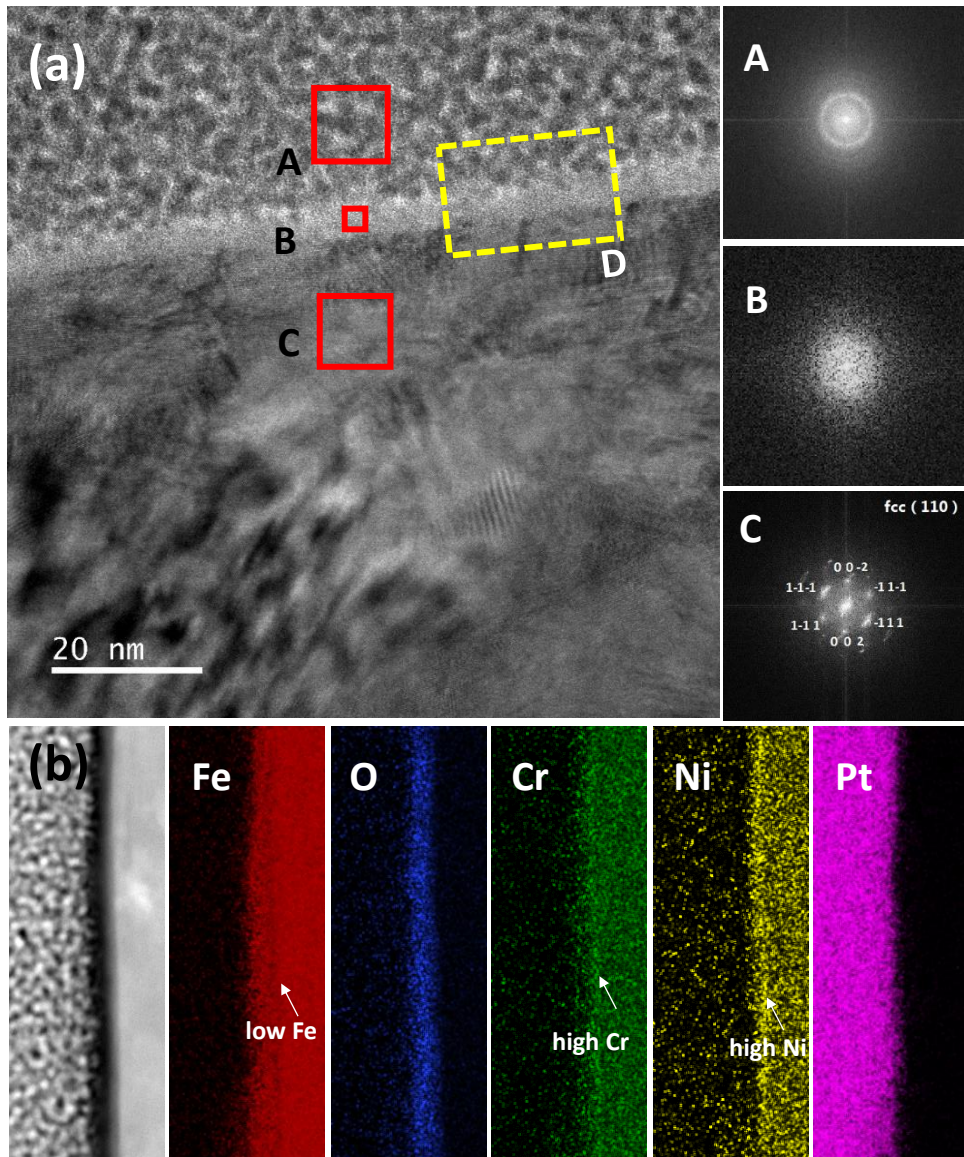
Figure 8. (a) An HR-TEM image of SLM 200 W 316L SS specimen in PBS solution at OCP, (b) a bright-field TEM image of the yellow square D in panel a and a STEM-EDX mapping profile of main matrix elements (Fe, O, Cr, Ni, Pt).

An EDS line scan across the entire passive film (through the red arrow) was performed to further analyse the elemental composition, as shown in Figure 9. It is interesting to note that the oxygen content was uniformly distributed across the outer passive film for SLM 200 W 316L SS compared with wrought 316L SS, suggesting the preferential formation of oxides by SLM manufacturing. These results were consistent with the XPS as shown in Figure 5. The decrease of oxygen weight fraction in the inner layer was observed, as well as the increase of chromium and nickel content at the material interface.

302

Figure 9. STEM image and EDS line profiles along the red arrow in the STEM image of the cross-sectional TEM sample of SLM 200 W 316L at OCP in PBS solution.
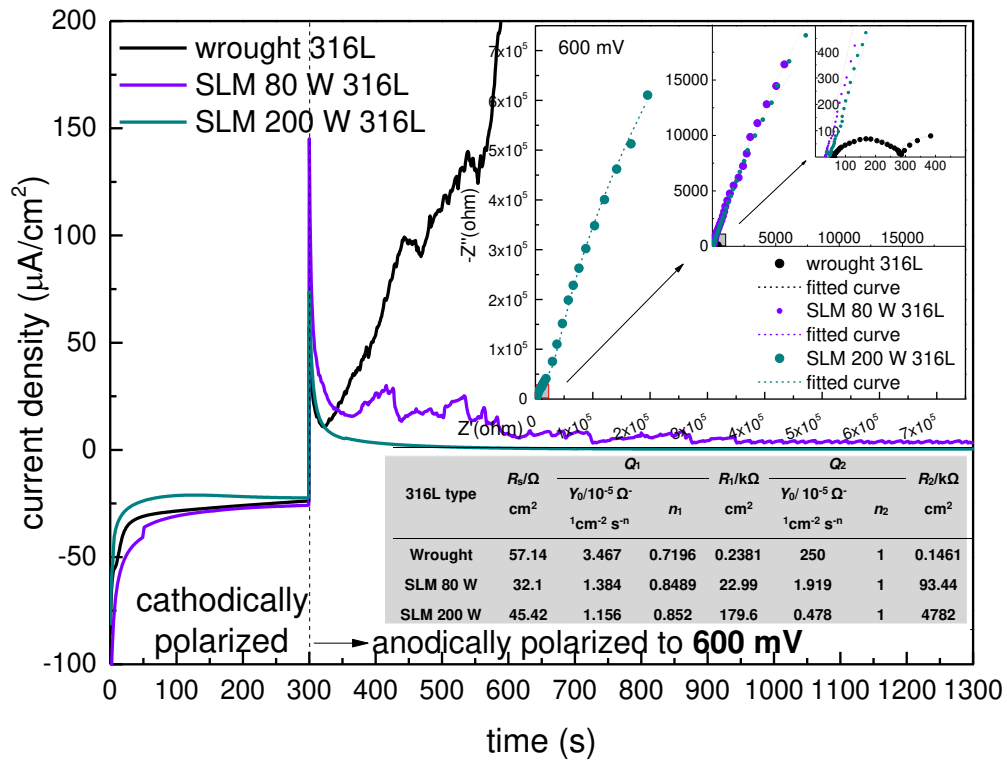
305

3.5 Effect of applied potentials on the passive film

To evaluate the interfacial reactions at the material interface, the current density response and EIS measurements for wrought and SLM 316L SS with applied potentials of 200 mV, 400 mV, and 600 mV vs. Ag/AgCl were recorded as shown in Figure S1 and Figure 10. The SLM 316L SS at 200 W laser power showed the best corrosion resistance, followed by SLM 316L SS at 80 W and the wrought 316L SS was the worst. For the polarization potential of 600 mV vs. Ag/AgCl, which was far beyond the passivation region for the wrought 316L but still in the passivation region for the SLM materials, the values of R_2 for SLM materials were orders of magnitude higher than that of the wrought 316L SS and indicated the best corrosion resistance under 600 mV vs. Ag/AgCl of the applied potential.

316L type	R_s/Ω cm²	Q_1		$R_1/k\Omega$ cm²	Q_2		$R_2/k\Omega$ cm²
		$Y_0/10^{-5}\,\Omega^{-1}$cm^{-2} s^{-n}	n_1		$Y_0/10^{-5}\,\Omega^{-1}$cm^{-2} s^{-n}	n_2	
Wrought	57.14	3.467	0.7196	0.2381	250	1	0.1461
SLM 80 W	32.1	1.384	0.8489	22.99	1.919	1	93.44
SLM 200 W	45.42	1.156	0.852	179.6	0.478	1	4782

Figure 10. The recorded EIS data of the samples immersed in PBS solution at 600 mV vs. Ag/AgCl.

3.6 Characterisation of the passive film at various applied potentials

XPS analyses were conducted to identify the chemical composition of the passive film formed on the SLM 200 W 316L SS. The peaks of Fe-2p 2/3, Cr-2p 2/3, and O-1s as shown in Figure 11 indicate the passive film compositions varied after applying 600 mV vs. Ag/AgCl. Both Cr-2p 2/3 and O-1s suggest the presence of more OH groups within the passive film after applying 600 mV vs. Ag/AgCl compared to OCP conditions. Considering the fast dissolution at high polarisation potential [39], the passivation ability of SLM produced 316L SS indicates the rapid formation and stability of the passive film at the sample surface. More structural relaxation compounds such as OH groups were observed within the passive film and the iron atoms tended to be present in high valence chemical states as shown in Figure 11.
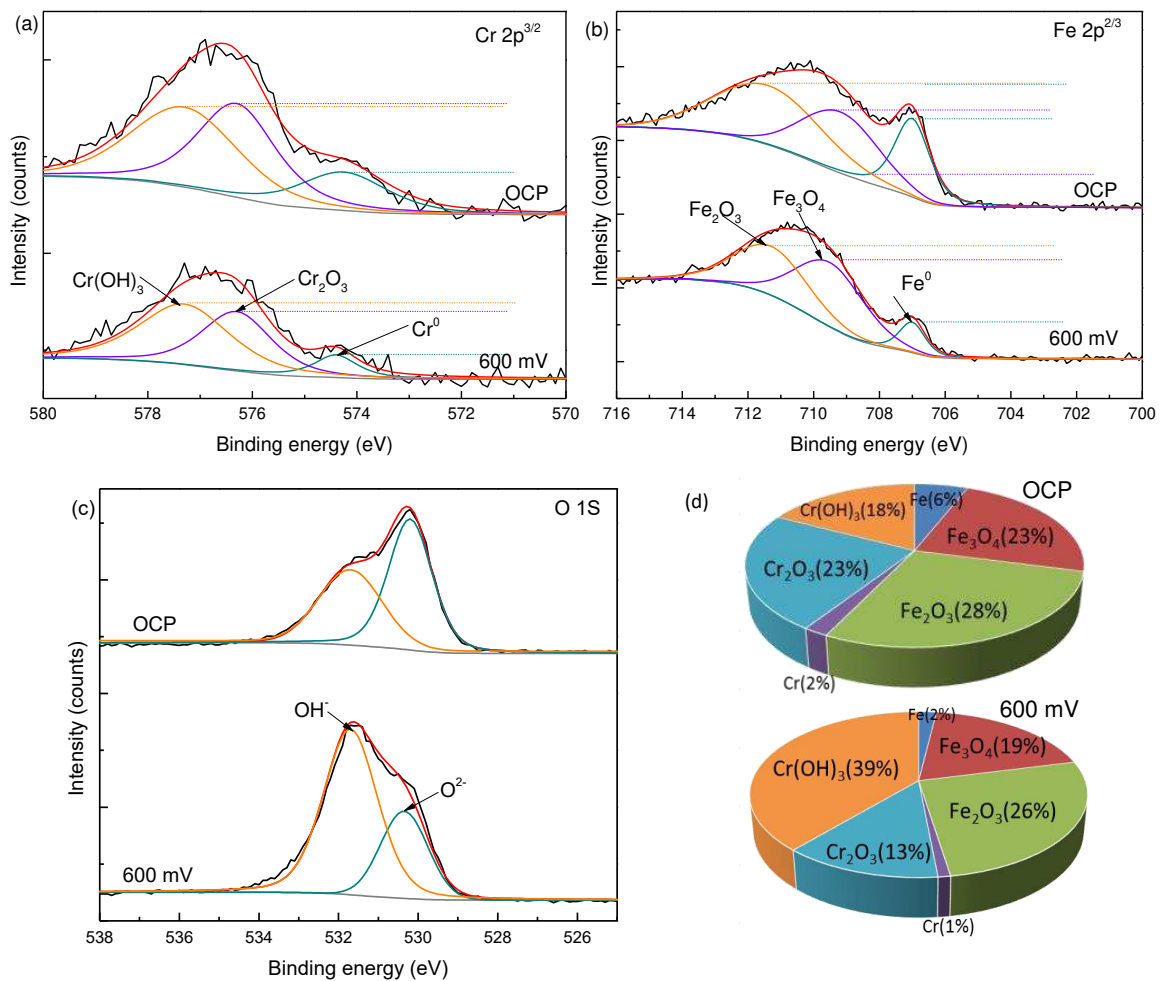
Figure 11. XPS results of the passive film formed on SLM 200 W 316L in PBS solution at OCP and 600 mV vs. Ag/AgCl: (a) Cr-2p 3/2, (b) Fe-2p 3/2, and (c) O-1s and (d) quantitative analysis.

Figure 12 shows images for another TEM sample which was prepared by subjecting the sample to potentiostatic control of 600 mV vs. Ag/AgCl to compare the film structure and elemental compositions within the passive film to that of OCP condition (Figure 8). The thickness of the passive film was increased to 7.6 nm and covers the entire substrate as shown in Figure 12a. The lattice structure of the passive film was further analysed by live FFT pattern taken from the square regions A, B, and C in HR-TEM image. The FFT patterns reflected from the substrate and sputter-coated Pt layer were crystalline and poly-crystalline, respectively. The passive film was a homogenous layer structure. The detected white dots in FFT images of the region B matched well with that detected in region C, which suggests nanocrystals with FCC structure were embedded in the passive films.

The STEM and EDS mapping profiles are shown in Figure 12b representing the elemental compositions within the passive film formed on the surface. Like the OCP-formed passive film, the presence of Fe, O, Ni, and Cr were detected in the passive layer, and the Cr and Ni were accumulated

345   in the inner layer. However, the enrichment of Cr expanded to the outer passive layer.
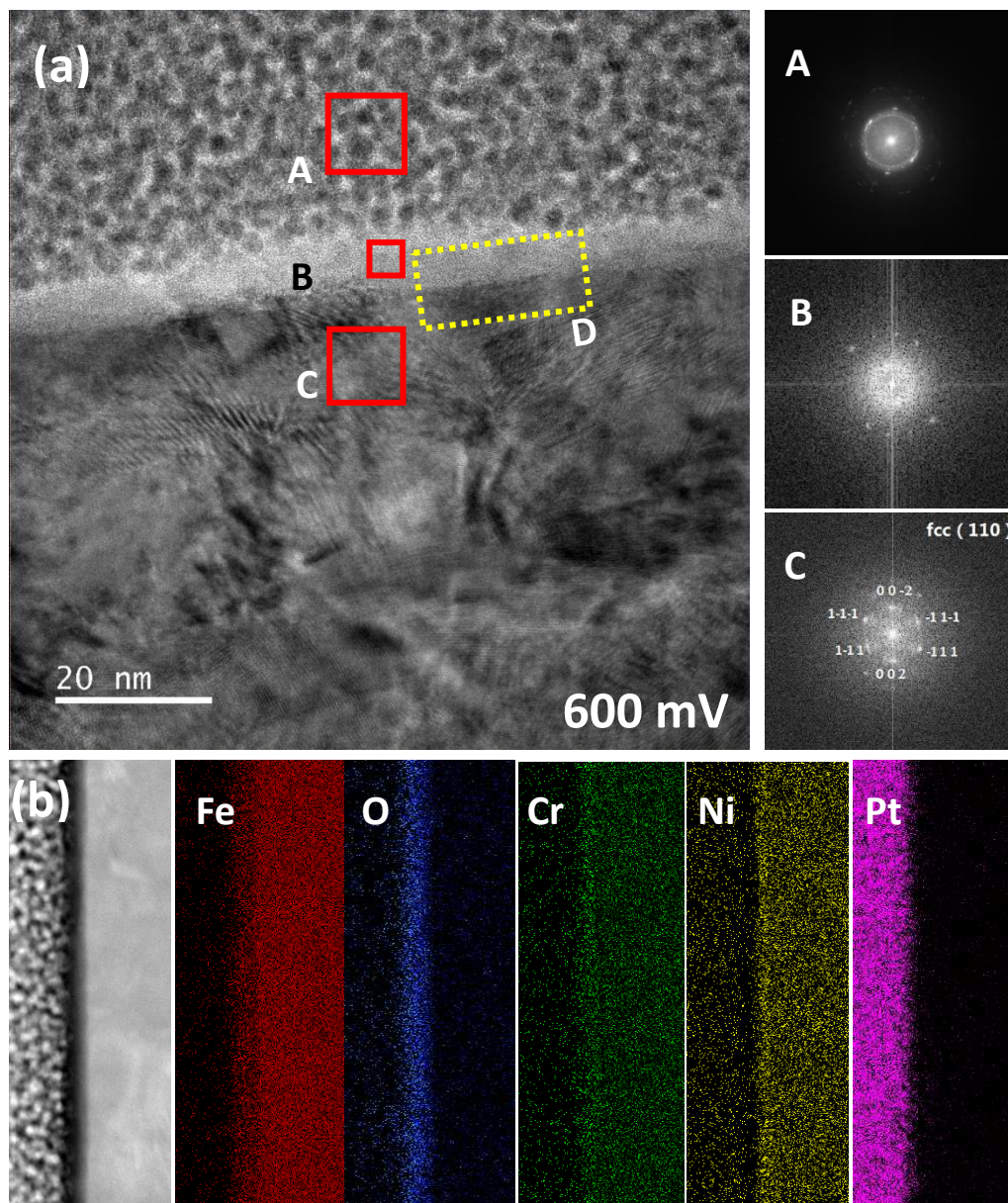

346

347   **Figure 12. (a) An HR-TEM image of SLM 200 W 316L SS specimen after polarisation in PBS**
348   **solution at 600 mV vs. Ag/AgCl, (b) a bright-field TEM image of the yellow square D in panel a**
349   **and a STEM-EDX mapping profile of main matrix elements (Fe, O, Cr, Ni, Pt).**

350

351   To further determine the elemental compositions within the passive film at 600 mV vs. Ag/AgCl

352   applied potential, an EDS line scan was conducted. As shown in Figure 13, the iron content was

353   detected within the passive film compared to the passive film formed at OCP condition in Figure 9.

354   Also, the chromium content increased to align with the increase in oxygen, which suggests the

355   proportion of oxides and hydroxides is dominates within the passive film for the sample was

356   polarised to 600 mV vs. Ag/AgCl potential.
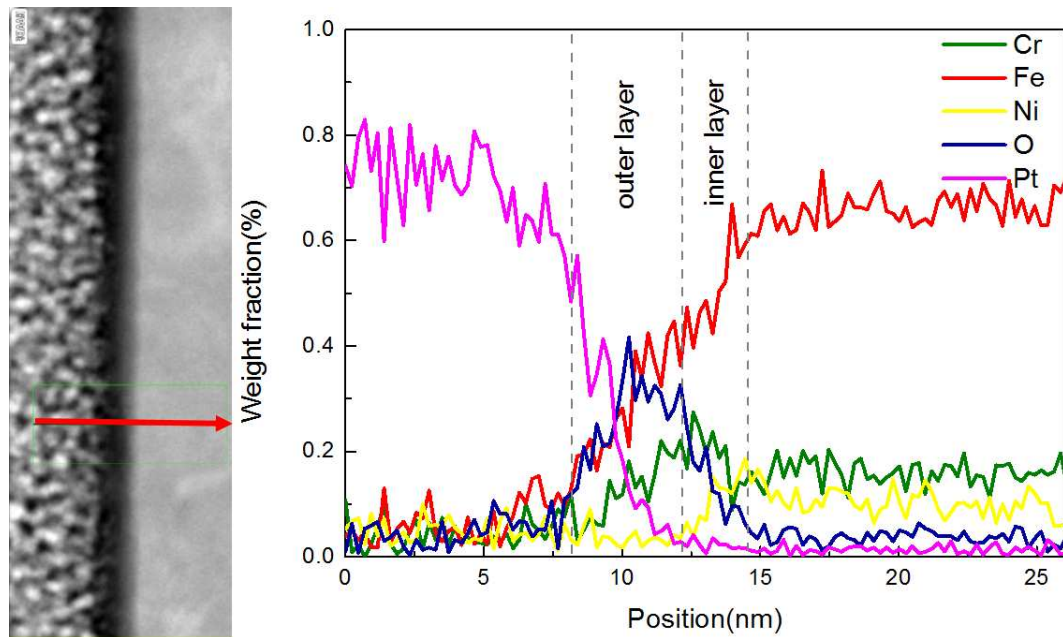
Figure 13. STEM image and EDS line profiles along the red arrow in the STEM image of the cross-sectional TEM sample of SLM 200 W 316L at 600 mV vs. Ag/AgCl.

4. Discussion

4.1 Superior passivation behaviour for SLM 200 W 316L SS at OCP condition

By the comparison of the structural perspective for the passive films, the passive layer formed on both wrought 316L and SLM 316L SS contained a Cr/Ni-rich inner layer. However, the Cr_2O_3/$Cr(OH)_3$ ratio for SLM 200 W 316L SS was higher than the wrought 316L SS, presenting a stabilised outer layer with better corrosion resistance. It was widely accepted that the presence of Cr_2O_3 coexists with $Cr(OH)_3$ and can act as the main barrier against corrosion and $Cr(OH)_3$ can be formed via consumption of Cr_2O_3 [40]. The increased ratio of Cr_2O_3/$Cr(OH)_3$ within the passive film formed on SLM 316L SS indicates a preference to the formation of Cr_2O_3 on the matrix and a preference of (110) facets.

Refer to Figure 2, the XRD results show the contrasting preferential Miller phase of (110) for SLM 316L SS compared to the (111) for wrought 316L SS. A hypothesis is proposed for the work of separation, where the presence of Cr_2O_3 formed on SLM 316L SS surface is different to that of wrought 316L SS. To prove the work of separation difference, first-principle computations to model the cohesion between passive film and the steel substrate (wrought 316L and SLM 316L SS) were performed. The main component of Fe and Cr_2O_3 was selected to represent as 316L SS substrate and the passive film, respectively [41]. The supercells constructed for the simulation contain the pure metal structure, oxide structure, and vacuum layer, respectively. The cleave surfaces of pure metal,

379 which were (110) and (111), enabled a quantification of the stability to the formation of the passive

380 film as illustrated in Figure 14.
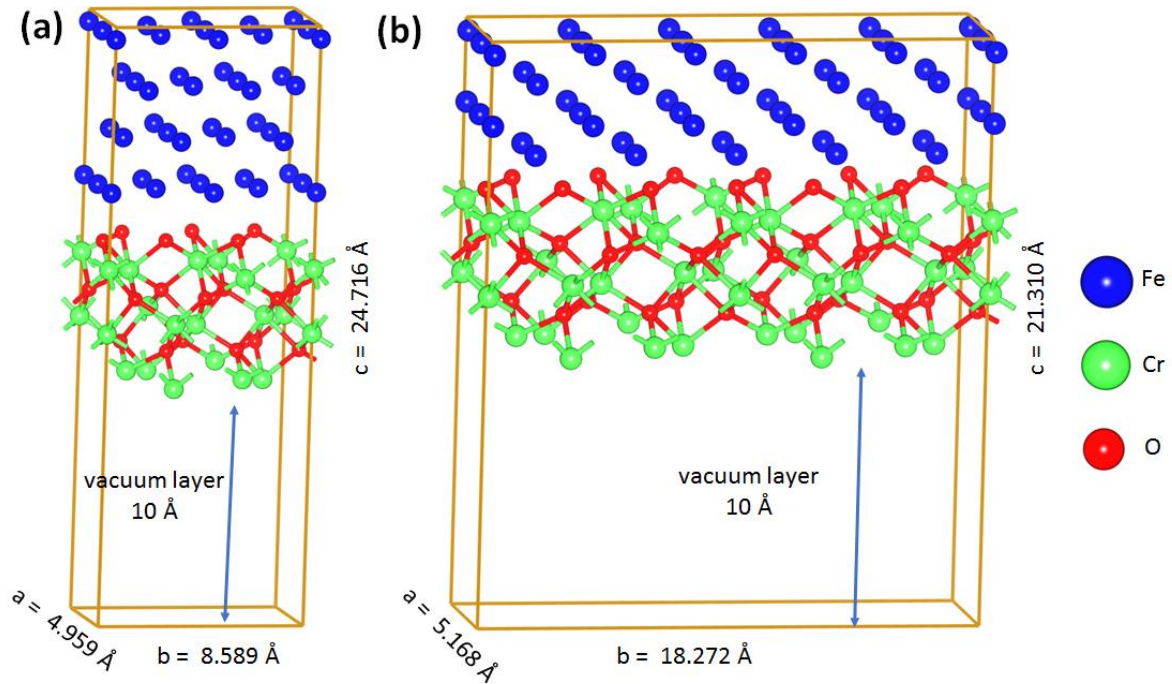
382 **Figure 14. Interface models of (a) Fe (111)/Cr₂O₃ and (b) Fe (110)/Cr₂O₃. The blue balls represent**
383 **Fe atoms, the green and red ball-sticks represent Cr and O atoms, respectively.**

385 The work of separation (W_{sep}) is well regarded as the reversible work needed to separate the

386 interface into two free surfaces, and the larger value of W_{sep} indicated a higher strength of interface

387 cohesion. W_{sep} of each Fe-Cr₂O₃ interface is calculated below [41,42]:

$$W_{sep} = \frac{E_{Fe} + E_{Cr_2O_3} - E_{tot}}{A}$$ (3)

389 Where E_{tot} (J) is the total energy of Cr₂O₃ and Fe interface, E_{Fe} (J) and $E_{Cr_2O_3}$ (J) represent

390 energies of free Fe and Cr₂O₃ surface layers after moving the Cr₂O₃ and Fe layers, respectively, and

391 A (Å²) is interface area of Fe-Cr₂O₃ interface.

392 As shown in Table S1, the Fe (110)/Cr₂O₃ interface was higher W_{sep} than that of Fe (111)/Cr₂O₃

393 interface, suggesting that Cr₂O₃ is energetically more prone to stay on Fe (110) surface compared to

394 the Fe (111) surface, thus confirming that the metal/passive film interface of SLM 200 W 316L SS

395 had better bonding energy. We suggest here that at least partly this explains why it is hard to

396 breakdown the passive film and why the SLM 316L exhibits better corrosion resistance than wrought

397 316L SS.

399 **4.2 Superior breakdown potential for the passive film formed on SLM 200 W 316L SS**

400 According to Figure 3, there is a potential range with notably improved passivation behaviour for

401 SLM 316L SS. The growth of the passive film is followed by metal dissolution promoted by the

402 potential reading more positive values until reaching a certain value [43]. For wrought 316L SS, this

403 threshold potential was close to 400 mV vs. Ag/AgCl, while the SLM 316L SS raised this potential to

404 ~ 1100 mV vs. Ag/AgCl.

405 During the exposure process of 316L SS samples in PBS solution, the steel matrix experienced metal

406 dissolution which promoted the initial formation of the inner Cr_2O_3-rich layer and subsequently

407 caused the formation of the outer passive layer [44]. It was reported that the growth of passive film

408 involved the transport of metal ions from the matrix. The passive film would attain dynamic

409 equilibrium as a barrier layer as the passive film growth rate was faster than the dissolution

410 processes. With the increase of the applied potential, this induced faster transport of oxygen ions

411 through the barrier, which requires faster metal ion transport to maintain a stable passive film

412 growth. For the wrought 316L SS, the undersupply of metal ions would cause the degradation of

413 both capacitance and resistance characteristics of the passive film at 600 mV vs. Ag/AgCl.

414 Based on the values of Y_0, R, and n of wrought 316L, SLM 80 W 316L, and SLM 200 W 316L from

415 the equivalent circuit (Figure 10) at the various applied potentials, the capacitance of the inner

416 (C_{inner}) and outer (C_{outer}) interface can be calculated via the following equations [45]:

$$C_{inner} = \frac{(Y_{0(Q2)} \cdot R_2)^{1/n}}{R_2} \tag{4}$$

$$C_{outer} = \frac{(Y_{0(Q1)} \cdot R_1)^{1/n}}{R_1} \tag{5}$$

419 The total capacitance of passive film (C) was then calculated and the results were shown in Figure

420 15 with R_{tot}.

$$C = C_{outer} + C_{inner} \tag{6}$$

422 Figure 15 indicates the SLM 200 W 316L has the smallest C values and largest R_{tot} values compared

423 to that of wrought 316L at each applied potential.

424 Consider the passive film as a parallel plate capacitor, its C value is related to the dielectric constant

425 of steady-state film thickness (ε) and estimated from the parallel plate capacitor expression [46]:

$$C = \frac{\varepsilon \, \varepsilon_0 A}{L_{SS}} \tag{7}$$

427 where L_{SS} is the passive film thickness, ε is the dielectric constant of steady-state film, ε_0 is the

428 vacuum permittivity (8.854 $\times$ 10^{-14} F·cm^{-1}), and A is the exposed area (1 cm²).

429 From the structural perspective, the thicknesses of passive films at OCP for the wrought 316L SS and

430 SLM 316L SS at 200 W are 6.3 nm and 4.6 nm respectively. A higher C value at OCP indicates the high

431 value of ε which has been reported to be associated with its hydrated nature [47]. The existing

432 hydroxide absorption fills the nanometer-scale pores of the inner layer and precipitates as the outer

433 layer, established to be less compact and protective than chromium oxide. According to the previous

434 discussion, the inner passive layer of SLM 316L SS which mainly consists of oxides is found to inhibit

435 the dissolution more effectively than the passive layer formed on wrought 316L SS, verified by their

436 lower C values and much higher R_{tot} values.

437 The sharply increased C value for wrought 316L SS at 600 mV vs. Ag/AgCl corresponded to the

438 breakdown of the passive film. The porous film increased the surface area and involved the H_2O with

439 a higher dielectric constant in the film, resulting in a particularly C value of 2505.3 $\mu F/cm^2$. However,

440 for the SLM 316L SS, the values of C remained below 100 $\mu F/cm^2$ even at the high applied potential

441 of 600 mV vs. Ag/AgCl, especially for the SLM 200 W 316L samples.

442 According to the results confirmed by XPS, the passive film formed on SLM 200 W 316L SS at a high

443 applied potential of 600 mV vs. Ag/AgCl contains a higher content of hydroxides, which resulting in

444 a high ε value associated with an increased L_{SS} value for the passive film (confirmed to be thicker

445 from 4.6 nm to 7.6 nm, confirmed via TEM) and led to the similar C values at both OCP and 600 mV

446 conditions.
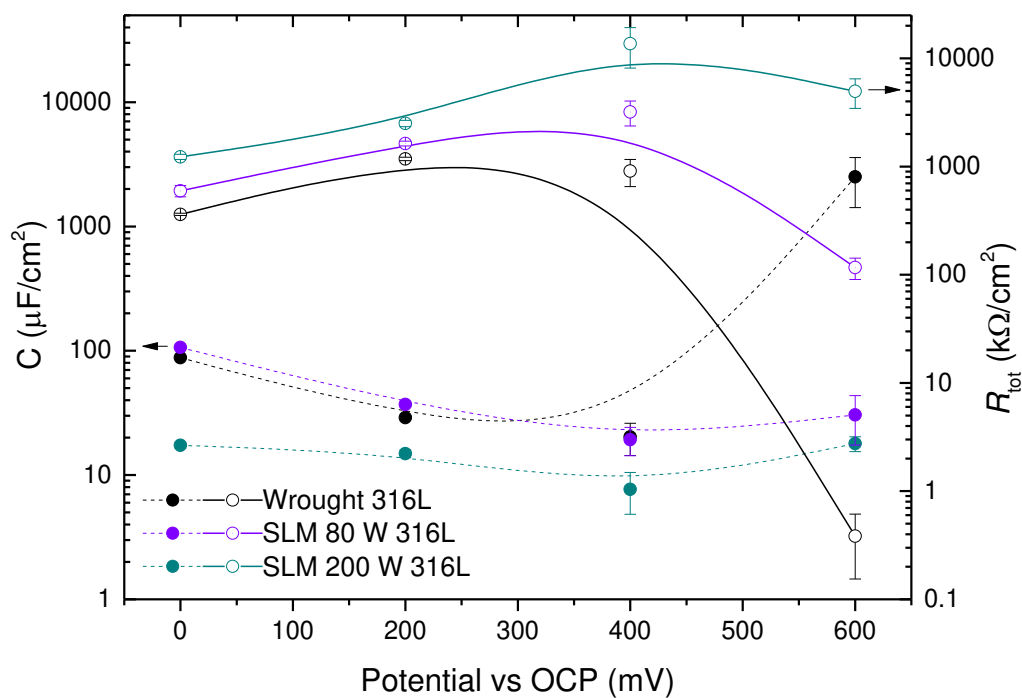
447
448 **Figure 15. Film capacitance and resistance of wrought 316L, SLM 80 W 316L, and SLM 200 W**
449 **316L at the various potentials.**

450 It was proposed that the passive film breakdown occurred when the film pressure exceeds a critical

451 value [26,48,49]. According to the previous papers, the pressure within the passive film was

452 generated as a consequence of the vacancies caused by the undersupply of metal cations at the

453 metal/passive film interface. For wrought 316L SS, the applied positive potential of 600 mV vs.

454 Ag/AgCl resulted in the film pressure exceeding the critical value and caused the passive film to

455 locally collapses (Figure 3). However, for SLM 200 W 316L SS, the high-resolution TEM image as

456 shown in Figure 15 confirms that the passive film was still continuous and compact at 600 mV vs.

457 Ag/AgCl. The embedded substrate as shown in Figure S2 verified the passive film for SLM 200 W

458 316L SS at a high polarised potential, indicating the possible transport of cations pass way and

459 suggesting the increased grain boundaries release the pressure within the passive film and stabilised

460 the passive film on the surface. The effect of residual stresses on passivity, especially related to

461 capacitance measurements on the passive film is our future focus.

462

463 ***4.3 Effect of the microstructure on the passivation behaviour***

464 It has been revealed that the grain size refinement improved the passivation behaviour based on the

465 promoted diffusion rate via the increased grain boundary paths [32,44]. SLM 316L SS showed the

466 features of the multitude of grain boundaries and sub-grain boundaries, providing more paths for

467 cation transport to the interface between the substrate and the amorphous zone, and avoiding the

468 generation of vacancies. Therefore, for the high polarised potentials, both grain boundaries and sub-

469 grain boundaries acted as efficient and active sites for the growth of oxides on the surface of SLM

470 316L SS, which accelerated the formation and diffusion processes and maintained the passive film

471 in a passive state.

472 It was suggested that the increase in the grain boundaries resulted in the improved passivation

473 behaviour and maintaining the material under the passivation state. However, in an active condition,

474 the increasing grain boundaries would promote the dissolution processes thus aggravating corrosion.

475 Ralston et al. [31] systematically summarised the relationship between corrosion rate (i_{corr}) and

476 grain size (*gs*) which observed as below:

$$i_{corr} = A + B \cdot gs^{-0.5} \tag{8}$$

478 Where constants A and B are related to the corrosion condition and material characteristics,

479 respectively. The value of B is determined by the corrosion behaviour, it assumes a negative value

480 under the passivation condition, whereas it turns to positive at non-passivating state [31]. In this

work, the A values for both wrought and SLM 316L SS are the same (PBS solution at 37°C), whereas the B values depend on the applied potentials. Under the potential below 400 mV vs. Ag/AgCl, B is negative and the relatively small grain sizes (gs) of the SLM 316L SS give an advantage of reducing i_{corr}. However, wrought 316L SS turned from passive to active state at high polarised potential of 600 mV vs. Ag/AgCl which indicated the value of B became positive (wrought 316L SS has large grain sizes) and consequently obtained a high i_{corr}. Therefore, SLM 316L SS stayed in passivation state over a wide potential range, corresponding a stable negative value of B and depressed i_{corr}.

5. Conclusions

In summary, the passivation behaviour of wrought 316L SS and SLM 316L SS was systematically investigated. The evolution of passive film at elevated potential was evaluated by structure, composition and electrochemical properties.

- The SLM 316L SS showed preferential formation of Miller phases of (110) gamma austenite phase containing an abundance of sub-grain boundaries, and the intensity of (110) phase enhanced with increasing the laser power.
- The SLM 316L SS preferential formed Miller phases of (110) and this showed improved breakdown potential compared with wrought 316L SS. The SLM 316L SS maintained the passivation state at 600 mV vs. Ag/AgCl, where wrought 316L tended to produce a more porous film with poor protection. The superior passivation behaviour SLM 316L SS, especially at 200 W, was related to a higher ratio of $Cr_2O_3/Cr(OH)_3$ within the passive film at OCP in PBS solution.
- The (110) facets of the matrix have a higher W_{sep} value with Cr_2O_3 compare with Fe(111)/ Cr_2O_3, indicating that the inner layer for SLM 200 W 316L depressed separation of the passive film and provided an opportunity for the developing of the whole layer. Abundant grain/sub-gain boundaries of the SLM 316L SS promoted the growth of the passive film and kept the passive film for SLM 200 W 316L staying completeness at 600 mV vs. Ag/AgCl.

6. References

[1] R. Misra, C. Nune, T. Pesacreta, M. Somani, L. Karjalainen, Understanding the impact of grain structure in austenitic stainless steel from a nanograined regime to a coarse-grained regime on osteoblast functions using a novel metal deformation–annealing sequence, Acta Biomater. 9 (2013) 6245–6258.

[2] C.-C. Shih, C.-M. Shih, Y.-Y. Su, L.H.J. Su, M.-S. Chang, S.-J. Lin, Effect of surface oxide properties on corrosion resistance of 316L stainless steel for biomedical applications, Corros. Sci. 46 (2004) 427–441.

[3] J.T. Scales, G. Winter, H. Shirley, Corrosion of orthopaedic implants: screws, plates and femoral nail-plates, J. Bone Joint Surg. Br. 41 (1959) 810–820.

[4] L. Navarro, J. Luna, I. Rintoul, Surface conditioning of cardiovascular 316l stainless steel stents: a review, Surf. Rev. Lett. 24 (2017) 1730002.

[5] T. Kamimura, K. Kashima, K. Sugae, H. Miyuki, T. Kudo, The role of chloride ion on the atmospheric corrosion of steel and corrosion resistance of Sn-bearing steel, Corros. Sci. 62 (2012) 34–41.

[6] D. Singh, R. Ghosh, B. Singh, Fluoride induced corrosion of steel rebars in contact with alkaline solutions, cement slurry and concrete mortars, Corros. Sci. 44 (2002) 1713–1735.

[7] C. of the E. Communities, Commission Directive 2004/96/EC of 27 September 2004 amending Council Directive 76/769/EEC as regards restrictions on the marketing and use of nickel for piercing post assemblies for purpose of adapting its Annex I to technical progress, J Eur Union. 301 (2004) 51–52.

[8] F. Nie, S. Wang, Y. Wang, S. Wei, Y. Zheng, Comparative study on corrosion resistance and in vitro biocompatibility of bulk nanocrystalline and microcrystalline biomedical 304 stainless steel, Dent. Mater. 27 (2011) 677–683.

[9] J. Lv, T. Liang, Improved corrosion resistance of 316L stainless steel by nanocrystalline and electrochemical nitridation in artificial saliva solution, Appl. Surf. Sci. 359 (2015) 158–165.

[10] T. Zhang, X. Jiang, X. Lu, S. Li, C. Shi, Corrosion wear of duplex stainless steels in sulfuric acid solution containing chloride, Corrosion. 50 (1994) 339–344.

[11] G. ZIJLSTRA, E.T. FABER, V. OCELÍK, J.T.M. DE HOSSON, THE GROWTH OF A PASSIVE FILM ON STEEL STUDIED WITH IN-SITU AFM, WIT Trans. Eng. Sci. 116 (2017) 23–29.

[12] Y. Kok, R. Akid, P.E. Hovsepian, Tribocorrosion testing of stainless steel (SS) and PVD coated SS using a modified scanning reference electrode technique, Wear. 259 (2005) 1472–1481.

[13] G. Sander, J. Tan, P. Balan, O. Gharbi, D. Feenstra, L. Singer, S. Thomas, R. Kelly, J. Scully, N. Birbilis, Corrosion of Additively Manufactured Alloys: A Review, Corrosion. 74 (2018) 1318–1350.

[14] A. Shahryari, S. Omanovic, J.A. Szpunar, Enhancement of biocompatibility of 316LVM stainless steel by cyclic potentiodynamic passivation, J. Biomed. Mater. Res. Part Off. J. Soc. Biomater. Jpn. Soc. Biomater. Aust. Soc. Biomater. Korean Soc. Biomater. 89 (2009) 1049–1062.

[15] T. Kurzynowski, K. Gruber, W. Stopyra, B. Kuźnicka, E. Chlebus, Correlation between process parameters, microstructure and properties of 316 L stainless steel processed by selective laser melting, Mater. Sci. Eng. A. 718 (2018) 64–73.

[16] F. Bartolomeu, M. Buciumeanu, E. Pinto, N. Alves, O. Carvalho, F. Silva, G. Miranda, 316L stainless steel mechanical and tribological behavior—a comparison between selective laser melting, hot pressing and conventional casting, Addit. Manuf. 16 (2017) 81–89.

[17] G. Sander, S. Thomas, V. Cruz, M. Jurg, N. Birbilis, X. Gao, M. Brameld, C. Hutchinson, On the corrosion and metastable pitting characteristics of 316L stainless steel produced by selective laser melting, J. Electrochem. Soc. 164 (2017) C250–C257.

[18] Z. Duan, C. Man, C. Dong, Z. Cui, D. Kong, X. Wang, Pitting behavior of SLM 316L stainless steel exposed to chloride environments with different aggressiveness: Pitting mechanism induced by gas pores, Corros. Sci. (2020).

557 [19] C. Man, C. Dong, T. Liu, D. Kong, D. Wang, X. Li, The enhancement of microstructure on the passive and pitting
558   behaviors of selective laser melting 316L SS in simulated body fluid, Appl. Surf. Sci. 467 (2019) 193–205.

559 [20] C. Man, Z. Duan, Z. Cui, C. Dong, D. Kong, T. Liu, S. Chen, X. Wang, The effect of sub-grain structure on
560   intergranular corrosion of 316L stainless steel fabricated via selective laser melting, Mater. Lett. 243 (2019)
561   157–160.

562 [21] A. Nazarov, V. Vivier, D. Thierry, F. Vucko, B. Tribollet, Effect of mechanical stress on the properties of steel
563   surfaces: scanning Kelvin probe and local electrochemical impedance study, J. Electrochem. Soc. 164 (2017)
564   C66–C74.

565 [22] Q. Chao, V. Cruz, S. Thomas, N. Birbilis, P. Collins, A. Taylor, P.D. Hodgson, D. Fabijanic, On the enhanced
566   corrosion resistance of a selective laser melted austenitic stainless steel, Scr. Mater. 141 (2017) 94–98.

567 [23] A.A. Aghuy, M. Zakeri, M.H. Moayed, M. Mazinani, Effect of grain size on pitting corrosion of 304L austenitic
568   stainless steel, Corros. Sci. 94 (2015) 368–376.

569 [24] M. Ziętala, T. Durejko, M. Polański, I. Kunce, T. P\lociński, W. Zieliński, M. \Lazińska, W. Stępniowski, T. Czujko,
570   K.J. Kurzyd\lowski, others, The microstructure, mechanical properties and corrosion resistance of 316 L
571   stainless steel fabricated using laser engineered net shaping, Mater. Sci. Eng. A. 677 (2016) 1–10.

572 [25] A.H. Ettefagh, S. Guo, Electrochemical behavior of AISI316L stainless steel parts produced by laser-based
573   powder bed fusion process and the effect of post annealing process, Addit. Manuf. 22 (2018) 153–156.

574 [26] V. Cruz, Q. Chao, N. Birbilis, D. Fabijanic, P.D. Hodgson, S. Thomas, Electrochemical studies on the effect of
575   residual stress on the corrosion of 316L manufactured by selective laser melting, Corros. Sci. 164 (2020).
576   https://doi.org/10.1016/j.corsci.2019.108314.

577 [27] X. Lou, P.L. Andresen, R.B. Rebak, Oxide inclusions in laser additive manufactured stainless steel and their
578   effects on impact toughness and stress corrosion cracking behavior, J. Nucl. Mater. 499 (2018) 182–190.

579 [28] D. Kong, X. Ni, C. Dong, X. Lei, L. Zhang, C. Man, J. Yao, X. Cheng, X. Li, Bio-functional and anti-corrosive 3D
580   printing 316L stainless steel fabricated by selective laser melting, Mater. Des. 152 (2018) 88–101.

581 [29] J.R. Trelewicz, G.P. Halada, O.K. Donaldson, G. Manogharan, Microstructure and corrosion resistance of laser
582   additively manufactured 316L stainless steel, Jom. 68 (2016) 850–859.

583 [30] S. Krishnan, J. Dumbre, S. Bhatt, E.T. Akinlabi, R. Ramalingam, Effect of crystallographic orientation on the
584   pitting corrosion resistance of laser surface melted AISI 304L austenitic stainless steel, (2013).

585 [31] K. Ralston, N. Birbilis, C. Davies, Revealing the relationship between grain size and corrosion rate of metals,
586   Scr. Mater. 63 (2010) 1201–1204.

587 [32] S. Gollapudi, Grain size distribution effects on the corrosion behaviour of materials, Corros. Sci. 62 (2012)
588   90–94.

589 [33] X. Yue, L. Zhang, Y. Wang, S. Xu, C. Wang, M. Lu, A. Neville, Y. Hua, Evolution and characterization of the film
590   formed on super 13Cr stainless steel in CO2-saturated formation water at high temperature, Corros. Sci. 163
591   (2020) 108277. https://doi.org/10.1016/j.corsci.2019.108277.

592 [34] H. Mathieu, D. Landolt, An investigation of thin oxide films thermally grown in situ on Fe 24Cr and Fe 24Cr
593   11Mo by auger electron spectroscopy and X-ray photoelectron spectroscopy, Corros. Sci. 26 (1986) 547–559.

594 [35] P. Marcus, J. Grimal, The anodic dissolution and passivation of NiCrFe alloys studied by ESCA, Corros. Sci. 33
595   (1992) 805–814.

596 [36] G. Allen, M. T. Curtis, AJ Hooper, and P. M, Tucker J Chem Soc Dalton Trans. 14 (1974) 1525.

597 [37] V. Maurice, W. Yang, P. Marcus, X-Ray Photoelectron Spectroscopy and Scanning Tunneling Microscopy Study
598   of Passive Films Formed on (100) Fe-18Cr-13Ni Single-Crystal Surfaces, J. Electrochem. Soc. 145 (1998) 909–
599   920.

600 [38] I. Olefjord, B.-O. Elfstrom, The composition of the surface during passivation of stainless steels, Corrosion.
601   38 (1982) 46–52.

602 [39] A.I. Munoz, L.C. Julián, Influence of electrochemical potential on the tribocorrosion behaviour of high carbon

603   CoCrMo biomedical alloy in simulated body fluids by electrochemical impedance spectroscopy,
604   Electrochimica Acta. 55 (2010) 5428–5439.

605 [40] C.-O. Olsson, D. Landolt, Passive films on stainless steels—chemistry, structure and growth, Electrochimica
606   Acta. 48 (2003) 1093–1104.

607 [41] J. Qian, C. Wu, H. Gong, S. Zhou, Cohesion properties of W-ZrC interfaces from first principles calculation, J.
608   Alloys Compd. 768 (2018) 387–391.

609 [42] G. Ma, J. Fan, H. Gong, Fundamental effects of hydrogen on cohesion properties of Cu/W interfaces, Solid
610   State Commun. 250 (2017) 79–83.

611 [43] C.-O. Olsson, D. Landolt, Film Growth during Anodic Polarization in the Passive Region on 304 Stainless Steels
612   with Cr, Mo, or W Additions Studied with EQCM and XPS, J. Electrochem. Soc. 148 (2001) B438–B449.
613   https://doi.org/10.1149/1.1404969.

614 [44] B. Zhang, J. Wang, B. Wu, X. Guo, Y. Wang, D. Chen, Y. Zhang, K. Du, E. Oguzie, X. Ma, Unmasking chloride
615   attack on the passive film of metals, Nat. Commun. 9 (2018) 2559.

616 [45] Z. Feng, X. Cheng, C. Dong, L. Xu, X. Li, Passivity of 316L stainless steel in borate buffer solution studied by
617   Mott–Schottky analysis, atomic absorption spectrometry and X-ray photoelectron spectroscopy, Corros. Sci.
618   52 (2010) 3646–3653. https://doi.org/10.1016/j.corsci.2010.07.013.

619 [46] E. Sikora, D.D. Macdonald, Defining the passive state, Solid State Ion. 94 (1997) 141–150.

620 [47] T. Moffat, R. Latanision, An electrochemical and X-Ray photoelectron spectroscopy study of the passive state
621   of chromium, J. Electrochem. Soc. 139 (1992) 1869–1879.

622 [48] N. Sato, A theory for breakdown of anodic oxide films on metals, Electrochimica Acta. 16 (1971) 1683–1692.

623 [49] T. Hoar, The production and breakdown of the passivity of metals, Corros. Sci. 7 (1967) 341–355.

624